Article

JOURNAL OF
REINFORCED
PLASTICS &
COMPOSITES

Journal of Reinforced Plastics and Composites
29(22) 3309–3321

DOI: 10.1177/0731684410380148
jrp.sagepub.com
SAGE

Prestressed composite specimen for mixed-mode I/II cracking in laminated materials

András Szekrényes

Abstract

This article presents the mixed-mode I/II prestressed end-loaded split specimen for the fracture testing of composite materials. The system is based on the fact that one of the two fracture modes is provided by the prestressed state of the specimen, and the other one is increased up to fracture initiation using a testing machine. The novel beam-like specimen is able to provide any combination of the mode-I and mode-II energy release rates. A simple closed-form solution is developed using beam theory as a data reduction scheme and for the calculation of the energy release rates in the new configuration. The applicability and the limitations of the novel fracture mechanical test are demonstrated using unidirectional glass–polyester composite specimens. If only crack propagation onset is involved, then the prestressed mixed-mode beam specimen can be used to obtain the fracture criterion of transparent composite materials in the G_I–G_{II} plane.

Keywords

Delamination, double-cantilever beam, end-loaded split, beam theory

Introduction

The delamination fracture is one of the major damage modes in laminated composite materials. Considering the linear elastic fracture mechanics (LEFM),[1] three basic types of the interlaminar fracture are known: mode-I (opening), mode-II (sliding or in-plane shear), and the mode-III (tearing or anti-plane shear). The significant part of the literature deals with the mode-I, mode-II, and the mixed-mode I/II cases,[2–4] although the interest of the scientists is subsequently focused on the mode-III and mixed-mode I/II, II/III fractures too.[5–11]

The currently available mixed-mode I/II configurations were summarized in many papers.[3,4] Considering the mixed-mode I/II delamination, there are large number of fracture systems, such as the mixed-mode bending (MMB),[12–14] the asymmetric double-cantilever beam (DCB) specimen,[15,16] the DCB loaded with uneven bending moments (DCB–UBM),[17,18] the DCB specimen loaded by forces and moments,[19] and – among others – the Arcan[20–22] or compact tension shear specimen (CTS).[23,24] Without any doubt, the most effective one among them is the MMB specimen developed by Reeder and Crews.[12,13] The specimen is able to provide any mode ratio; however, the complex fixture involved by the MMB specimen is a drawback of the test.

As an alternative possibility, the mixed-mode I/II prestressed end-notched flexure ($PENF_{I/II}$) system was published in 2006[25] and probably it is the simplest configuration, which is ever developed. The system requires only a three-point bending setup and few steel rollers with different diameters. The rollers are used to prestress the specimens by fixing the crack opening displacement (COD); then we can put the specimen into a three-point bending setup and the mode-II energy release rate (ERR) can be increased up to the

Department of Applied Mechanics, Budapest University of Technology and Economics, Budapest.

Corresponding author:
András Szekrényes, Department of Applied Mechanics, Budapest University of Technology and Economics, H-1111 Budapest, Műegyetem rkp. 5, Building MM, Hungary
Email: szeki@mm.bme.hu

critical value. In Szekrényes[25], the applicability and the drawbacks of the test are demonstrated using glass–polyester composite specimens. It was shown that the mode ratio changes with the crack length and the external load, although this change is estimated to be small. An improved beam theory (IBT) scheme was found to be accurate for the data reduction and the fracture envelope of the material was obtained using the well-known power and Williams' criteria.

The method of prestressed composite beams was later extended to mixed-mode II/III[26] and I/III cases[27] too.

The aim of this article is to develop a similar mixed/mode I/II configuration, which makes it possible to test the material at relatively large crack lengths. This is the reason for why the combination of the end-loaded split (ELS),[28,29] and the DCB,[30,31] is realized. While in the case of the $PENF_{I/II}$ the crack length range is limited by the central load introductor, in the ELS specimen the end load does not make any restrictions to the crack length. The $PELS_{I/II}$ is based on the same concept as the $PENF_{I/II}$. A steel roller is inserted between the specimen arms and the built-in prestressed specimen is loaded by a force at the end. The applicability and the advantages/drawbacks of the test are demonstrated by finite element (FE) calculations and experiments. Finally, a fracture envelope is obtained in the G_I–G_{II} plane.

The PELS specimen for mixed-mode I/II cracking

The $PELS_{I/II}$ specimen is the combination of the DCB and ELS specimens. As it is shown in Figure 1, P_{DCB} is the load related to the mode-I part of the ERR caused by a steel roller (Figure 1(c)), while P_{ELS} is the load related to the mode-II loading. For the analysis of the $PELS_{I/II}$ configuration, we superimpose the solutions of the DCB and ELS specimens. In a previous work, the IBT solutions for the DCB and ELS specimens were presented.[32]

The compliance of the DCB specimen can be expressed as:[32]

$$C_{DCB} = \frac{8a^3}{bh^3E_{11}} + \frac{2a^3}{bh^3E_{11}}\left(f_{W1} + f_T + \frac{f_{SV}}{2}\right) \quad (1)$$

where a is the crack length, b the specimen width, h the half thickness, and E_{11} the flexural modulus of the specimen. Furthermore, f_{W1} is obtained from the Winkler–Pasternak foundation, f_T from transverse shear and f_{SV} accounts for the Saint–Venant effect:

$$f_{W1} = 5.07\left(\frac{h}{a}\right)\left(\frac{E_{11}}{E_{22}}\right)^{\frac{1}{4}} + 8.58\left(\frac{h}{a}\right)^2\left(\frac{E_{11}}{E_{22}}\right)^{\frac{1}{2}} + 2.08\left(\frac{h}{a}\right)^3\left(\frac{E_{11}}{E_{22}}\right)^{\frac{3}{4}}, \quad (2)$$

$$f_T = \frac{1}{k}\left(\frac{h}{a}\right)^2\left(\frac{E_{11}}{G_{12}}\right), \quad (3)$$

$$f_{SV} = \frac{12}{\pi}\left(\frac{h}{a}\right)\left(\frac{E_{11}}{G_{12}}\right)^{\frac{1}{2}}, \quad (4)$$

where E_{22} is the transverse modulus in the y direction, G_{12} the shear modulus of the material in the x–y plane and $k = 5/6$ the shear correction factor. The mode-I ERR of the DCB specimen can be obtained using the Irwin–Kies expression:[1]

$$G_C = \frac{P^2}{2b}\frac{dC}{da}, \quad (5)$$

that is:

$$G_I = \frac{P_{DCB}^2 a^2(12 + f_{W2} + f_T + f_{SV})}{b^2h^3E_{11}}, \quad (6)$$

where P_{DCB} is the external load, and:

$$f_{W2} = 10.14\left(\frac{h}{a}\right)\left(\frac{E_{11}}{E_{22}}\right)^{\frac{1}{4}} + 8.58\left(\frac{h}{a}\right)^2\left(\frac{E_{11}}{E_{22}}\right)^{\frac{1}{2}}. \quad (7)$$

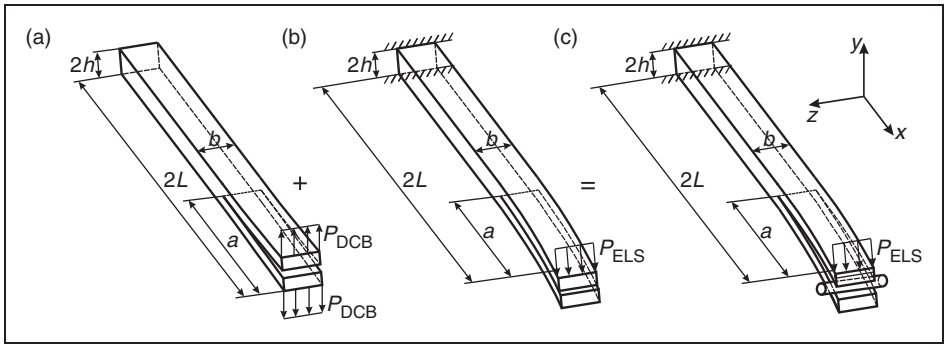

Figure 1. The mixed-mode I/II PELS specimen (c) as the superposition of the DCB (mode-I) (a) and ELS (mode-II) (b) specimens.

The COD (δ_{DCB}) of the specimen can be controlled by inserting a steel roller between the specimen arms. A reasonable assumption is that the COD is approximately equal to d_0. For this reason, we express the force which arises in the DCB specimen using Equation (1) and the definition of $C_{DCB} = \delta_{DCB}/P_{DCB}$:

$$P_{DCB} = \frac{bh^3 E_{11}\delta_{DCB}}{8a^3}\frac{1}{1+(f_{W1}+f_T+f_{SV}/2)/4}, \quad (8)$$

where $\delta_{DCB} = d_0$ is the diameter of the prestressing roller. Substituting Equation (8) into Equation (6) we obtain:

$$G_I^{DCB} = \frac{h^3 E_{11}\delta_{DCB}^2}{64a^4}\frac{[12+f_{W2}+f_T+f_{SV}]}{[1+(f_{W1}+f_T+f_{SV}/2)/4]^2}. \quad (9)$$

The improved solution for the ELS specimen's compliance is:[32]

$$C^{ELS} = \frac{3a^3+L^3}{2bh^3E_{11}} + \frac{L}{2bhkG_{13}} + \frac{3}{\pi}\frac{L^2}{2bh^2E_{11}}\left(\frac{E_{11}}{G_{13}}\right)^{\frac{1}{2}} + \\ + \frac{a^3}{2bh^3E_{11}}\left[0.98\left(\frac{h}{a}\right)\left(\frac{E_{11}}{G_{13}}\right)^{\frac{1}{2}} + 0.43\left(\frac{h}{a}\right)^2\left(\frac{E_{11}}{G_{13}}\right)\right], \quad (10)$$

and the ERR becomes:

$$G_{II}^{ELS} = \frac{P^2a^2}{4b^2h^3E_{11}}[9+f_{SH2}], \quad (11)$$

where f_{SH2} is obtained from the crack tip deformation:[32]

$$f_{SH2} = 1.96\left(\frac{h}{a}\right)\left(\frac{E_{11}}{G_{13}}\right)^{\frac{1}{2}} + 0.43\left(\frac{h}{a}\right)^2\left(\frac{E_{11}}{G_{13}}\right).$$

Finally, the mode ratio of the $PELS_{I/II}$ specimen is:

$$\frac{G_I}{G_{II}} = \frac{b^2E_{11}^2}{16}\left(\frac{h}{a}\right)^6\left(\frac{\delta_{DCB}}{P_{ENF}}\right)^2 \\ \times \frac{(12+f_{W2}+f_T+f_{SV})}{[1+(f_{w1}+f_T+f_{SV}/2)/4]^2}\frac{1}{(9+f_{SH2})}, \quad (12)$$

which depends on the crack length and the applied load also. All of the factors in Equation (12) have been defined before. The accuracy of the analytical solution has already been proven in previous papers.[25,32] However, some other questions should be clarified and these are detailed in the following sections.

The dependence of the mode ratio on the crack length can be investigated based on Equation (12). In Table 1, we calculated the mode ratio at $a = 105$ mm

Table 1. The changes in the mode ratio G_I/G_{II} in the case of inaccurate crack initiation detection if $a = 105$ mm

Δa	0.25	0.35	0.5	0.75	1	1.25	1.5	2
Difference (%)[a]	1.4	1.9	2.7	4.1	5.4	6.7	8.0	10.4

[a] $(G_I/G_{II}|_{a+\Delta a} - G_I/G_{II}|_{a=105})/(G_I/G_{II}|_{a=105})$.

using the following material properties: $E_{11} = 33$ GPa, $E_{22} = 7.2$ GPa, and $G_{12} = 3$ GPa. The geometrical properties are: $b = 20$ mm and $2h = 6.2$ mm. In the calculation, we subsequently increased the crack length by small increments until 2 mm. If the crack length is measured inaccurately, it has a moderate influence on the mode ratio. If $\Delta a = 1$ mm, then the expected error is 5.4%. This indicates that the accurate measurement of the crack length after crack initiation is important. During the experiments (in a later section), a transparent material is used, so that the crack initiation is easily identified within 0.5 mm.

If the crack opening is relatively large, then the crack lengths of the upper and lower specimen arms will be different from their original values. This is due to the fact that the contact point between the specimen arms and the roller is located at a distance of a_u^* and a_l^* instead of 'a' from the crack tip, as it is shown in Figure 2. We can calculate the distances, a_u^* and a_l^*, based on a simple geometrical analysis. According to Figure 2, we need to find the coordinates, a_u^* and a_l^*, where the derivative of $f_i(x) = \pm(x+2a)(x-a)^2/(4a^3)\cdot\delta_{DCB} + 1/2(4x^3 - 9a^2x - 3xL + 6a^3 + 2L^3)/(3a^3 + L^3)\cdot\delta_{ELS}$ (simple beam theory solution, $i = 1$ for the upper arm, the positive sign, $i = 2$ for the lower arm, negative sign) and $f_c(x) = ((\delta_{DCB}/2)^2 - x^2)^{1/2} + \delta_{ELS}$ (equation of a circle with diameter, δ_{DCB}) is the same. Table 2 shows the changes of the crack length, and the difference compared to the original crack length. In the worst case (if $d_0 = 13$ mm), we make a mistake of 1% in the crack length. A reasonable conclusion is that the change of the crack length is negligible.

A major question in a mixed-mode configuration is the estimation of the change in the mode ratio along the crack front, and its effect on the ERRs. To clarify this question, a FE model shown in Figure 3 is utilized. For the calculation, the ANSYS 12 package was used. The elastic properties of the models were: $E_{11} = 33$ GPa, $E_{22} = E_{33} = 7.2$ GPa, $G_{12} = G_{13} = G_{23} = 3$ GPa, and $\nu_{12} = \nu_{13} = \nu_{23} = 0.27$. The geometrical properties are: $b = 20.0$ mm, $2h = 6.2$ mm and the length of the models was $L = 150$ mm (Figure 1). The 3D model of the ELS specimen was built using linear eight-node solid brick elements. The imposed boundary conditions and the loading of the model are demonstrated in Figure 3. At the end of the specimen arms, the displacements shown in Figure 3 were imposed, where δ_{DCB} was equal to the actual roller diameter ($d_0 = 6$, 7, 8, 10, 12,

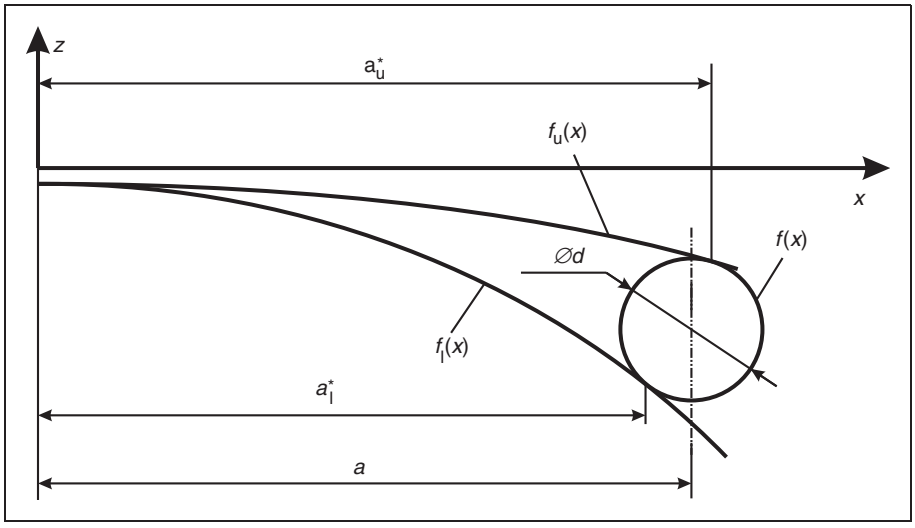

Figure 2. The effect of the prestressing roller on the crack length of the $PELS_{I/II}$ specimen.

Table 2. The changes in the crack length of the prestressed specimen with the steel roller diameter

δ_{DCB} (mm)	0	6	7	8	10	12	13
δ_{ELS} (mm)	19.4	16.1	12.8	11.0	8.8	5.6	4.2
a_u^* (mm)	105	106	105	105	105	105	105
Difference compared to $a = 105$ mm (%)	0.0	1.0	0.0	0.0	0.0	0.0	0.0
a_l^* (mm)	105.0	104	104	104	104	104	104
Difference compared to $a = 105$ mm (%)	0.0	−1.0	−1.0	−1.0	−1.0	−1.0	−1.0

a_u^*, the crack length of the upper arm; a_l^*, the crack length of the lower arm.

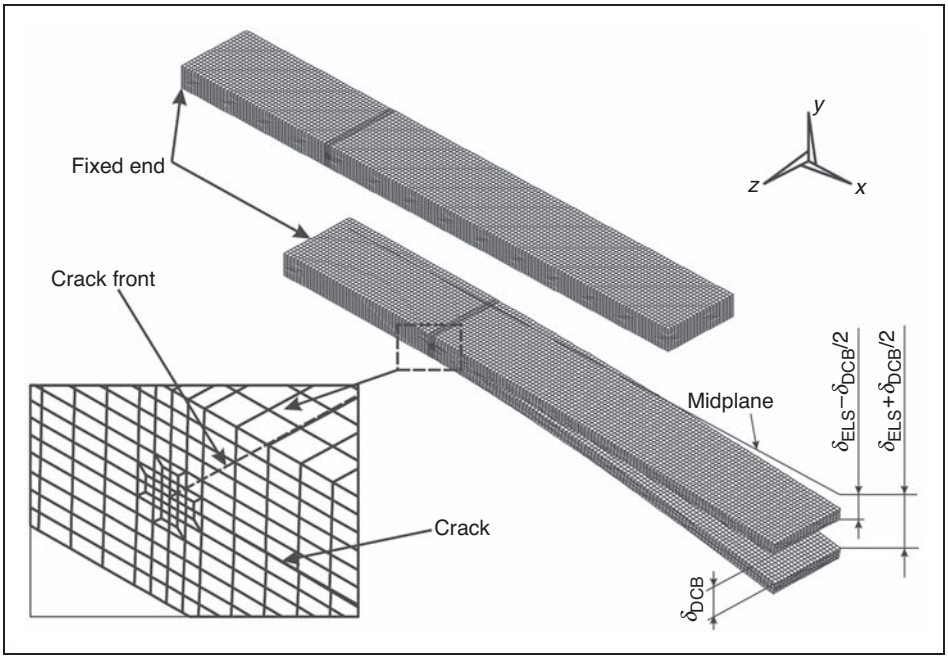

Figure 3. The applied boundary conditions of the $PELS_{I/II}$ specimen and the details of the FE model.

and 13 mm) and δ_{ELS} was the critical displacement of the $PELS_{I/II}$ specimen at crack initiation.

In the crack tip, a refined mesh was constructed and the mode-I and mode-II ERRs were evaluated by using the virtual crack-closure technique (VCCT),[33,34] the size of the crack tip elements were $\Delta x = \Delta y = 0.25$ mm and $\Delta z = 1$ mm (Figure 3, coordinate system).

Figures 4(a) and (b) and 5(a) show the distribution of the ERRs along the crack front in the case of $d_0 = 8$, 10, and 12 mm, while Figure 5(b) shows the variation of

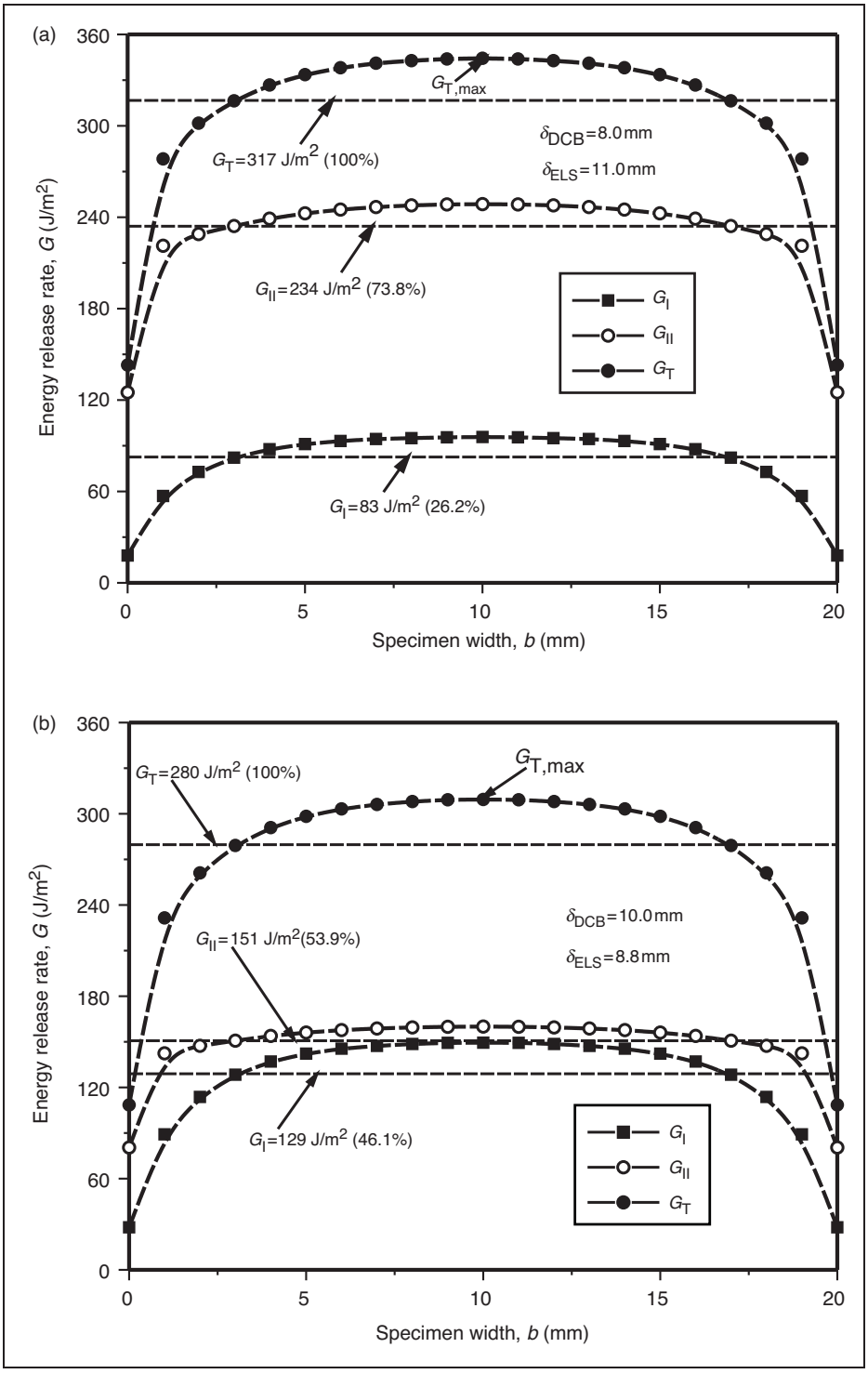

Figure 4. The distribution of the mode-I and mode-II ERRs along the crack front in the case of d_0=8.0 mm (a) and d_0 = 10.0 mm (b).

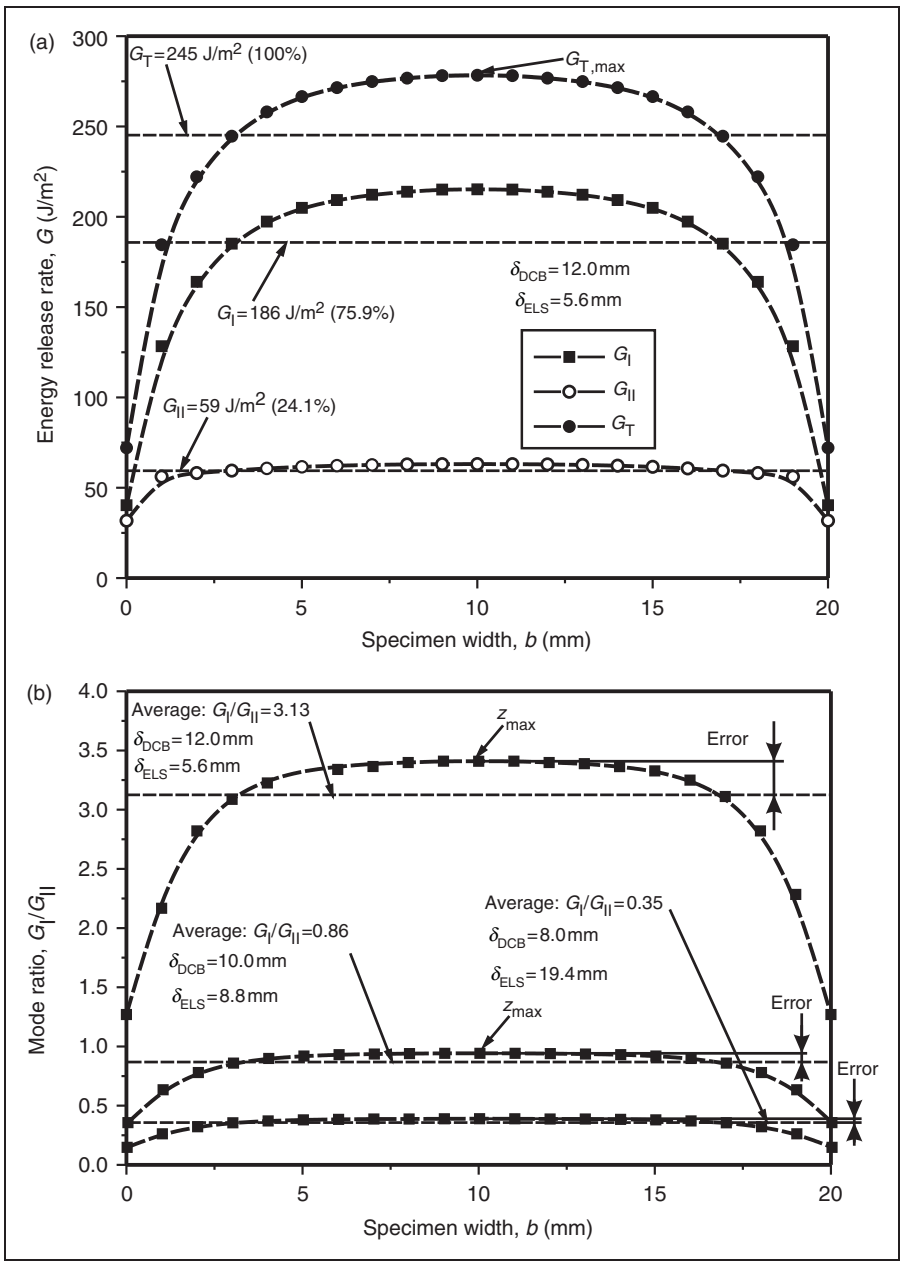

Figure 5. The distribution of the mode-I and mode-II ERRs along the crack front in the case of $d_0 = 12.0$ mm (a) and the variation of the mode ratio along the crack front if $d_0 = 8.0$, 10.0, and 12.0 mm (b).

the mode ratio in each case. The values of δ_{ELS} were determined based on crack initiation experiments (in a later section). As it is expected, the mode-I and mode-II ERRs have a symmetric distribution along the crack front (similarly to the results in[35]). In Figures 4(a) and (b) and 5(a) and (b), the average ERRs and mode ratios were obtained by dividing the integrated area under the curve by the specimen width. Table 3 shows the comparison of the IBT to the VCCT with respect to the average ERR and mode ratio. The IBT overestimates G_I at most with 4.3% and even G_{II} at most with 11.9%. This relatively significant difference is due to the fact that the FE model was loaded by imposed displacement, and the δ_{ELS} displacement was calculated based on the measured load–displacement slopes and the critical P_{ELS} values. The maximum difference in the mode ratio is 12.9%, which is the result of the rounding of G_I and G_{II}. Overall, this agreement is good and based on these results, the IBT is a possible data reduction scheme for the PELS$_{I/II}$ test.

Since the ERR varies along the crack front, that is, it is the highest at the center and the lowest at the specimen edges, it is obvious that the specimen possesses a curved crack front under crack propagation. As it is

Table 3. Comparison of the ERRs and mode ratios by beam and FE analysis

Roller diameter	d_0 (mm)	0 (ELS)	6	7	8	10	12	13	~15 (DCB)
Load at crack initiation	P_{ELS} (N)	103.1	82.6	70.8	61.9	48.3	31.3	22.5	0
Displacement at crack initiation	δ_{ELS} (mm)	19.4	16.1	12.8	11.0	8.8	5.6	4.2	0
G_I (J/m^2)	IBT[a]	–	48	65	85	132	190	223	412
	VCCT widthwise average[b]	–	47	63	83	129	186	218	395
	VCCT at z^c_{max}	–	54	73	96	149	215	253	457
	Difference (a–b)/b (%)	–	2.1	3.2	2.4	2.3	2.2	2.3	4.3
	Difference (a–c)/c (%)	–	−11.1	−11.0	−11.5	−11.4	−11.6	−11.9	−9.8
G_{II} (J/m^2)	IBT[a]	707	454	333	255	156	66	34	–
	VCCT widthwise average[b]	724	502	316	234	151	59	34	–
	VCCT at z^c_{max}	767	533	336	249	160	63	36	–
	Difference (a–b)/b (%)	−2.3	−9.6	5.4	9.0	3.3	11.9	0.0	–
	Difference (a–c)/c (%)	−7.8	−14.8	−0.9	2.4	−2.5	4.8	−5.6	–
G_I/G_{II}	IBT[a]	0	0.11	0.20	0.33	0.85	2.88	6.56	∞
	VCCT widthwise average[b]	0	0.09	0.20	0.35	0.85	3.15	6.41	∞
	VCCT at z^c_{max}	0	0.10	0.22	0.39	0.93	3.41	7.03	∞
	Difference (a–b)/b (%)	–	12.9	−2.1	−6.1	−1.0	−8.7	2.3	–
	Difference (a–c)/c (%)	–	4.4	−10.2	−13.5	−9.1	−15.6	−6.7	–

[a]IBT; [b]VCCT widthwise average; and [c]VCCT at z_{max}.

seen in Figure 5(b), it is not possible to produce a constant mode ratio along the crack front. Consequently, some assumptions are required considering the reduction of the experimental data. In the data reduction and the calculation of G and G_I/G_{II}, the widthwise average values will be adopted. To assess the possible errors (Figures 4(a) and (b) and 5(a)) in the calculation of G and G_I/G_{II} by the IBT we assume that the crack initiation takes place at the point where the total ERR (G_T) reaches the highest value. This point can be found always in the midpoint of the crack fronts marked by z_{max}. In Table 3, the ERRs and mode ratios are calculated by using the values by VCCT at z_{max} too and they are compared to the result of IBT. The difference in G_I is around 11.5%, while in the case of G_{II} the difference changes between 1% and 15%, which seems to be significant. On the contrary, the difference in the mode ratio is negligible in each case.

Although there are some errors in the analytical predictions of G_I and G_{II}, the mode ratio is accurately estimated by the IBT method, and we prefer the IBT as a data reduction scheme, because the FE analysis-based data reduction requires much computational time. Moreover, assumption is also required if we apply the VCCT to reduce the experimental data, and the IBT agrees excellently with the widthwise average G and G_I/G_{II}. It should be mentioned that a similar variation of the mode ratio could exist in the MMB system too.[12]

In the sequel, the details of the experimental work is presented.

Experiments

Material properties

The constituent materials of the E-glass–polyester composite were procured from Novia Ltd. The properties of the E-glass fiber are $E = 70$ GPa and $\nu = 0.27$, and the properties of the unsaturated polyester resin we applied are: $E = 3.5$ GPa and $\nu = 0.35$. Both were considered to be isotropic. The unidirectional ($[0^\circ]_{14}$) E-glass–polyester specimens with thickness of $2h = 6.2$ mm, width of $b = 20$ mm, and fiber–volume fraction of $V_f = 43\%$ were manufactured in a special pressure tool. A polyamide (PA) insert with thickness of 0.03 mm was placed at the midplane of the specimens to make an artificial starting defect. It should be highlighted that this film thickness is higher than the 0.013 mm recommended in the DCB and MMB test standards.[2,3]

A great advantage of the E-glass–polyester material used in this study is its transparency, which makes it possible to observe the crack initiation visually. The tool was left at room temperature until the specimens became dry. Then the specimens were removed from the tool and were further left at room temperature until 4–6 h. The specimens were cut to the desired length and were precracked in opening mode of 4–5 mm by using a sharp blade.

The flexural modulus of the material was determined from a three-point bending test with span length of $2L = 150$ mm using six uncracked specimens with

thickness of $2h = 6.2$ mm and width $b = 20$ mm. The flexural modulus was computed in accordance with simple beam theory expression: $\delta_{\text{bend}} = PL^3/(4bh^3E_{11})$, which is the displacement at the point of load introduction. The experiments resulted in $E_{11} = 33$ GPa. In fact, the shear deformation was not accounted for; however, its contribution to the displacement is quite small: $\delta_{\text{shear}} = PL/(4bhkG_{12})$. The additional properties were predicted from simple rules of mixture; in this way $E_{22} = E_{33} = 7.2$ GPa, $G_{12} = G_{13} = 3$ GPa, and $\nu_{12} = \nu_{13} = 0.27$ were obtained. Using these values, the ratio of the displacements from bending and shear deformation at the center of the specimens is: $(h/L)^2 \cdot E_{11}/(G_{12}k) = 0.0056$, that is, the amount of shear deformation is quite small and can be neglected. The material properties were used in the data reduction process.

DCB test

In the case of the DCB test (Figure 1(b)), we refer to previous fracture experiments[36] performed in the crack length range of $a = 20$–150 mm. It has been found that the critical ERR at crack initiation becomes independent of a, after 90 mm. The steady-state ERR was $G_{\text{IC}} = 412\,\text{J/m}^2$ evaluated by using an IBT scheme. This value will be used in the sequel.

ELS test

For the ELS measurements, four specimens were prepared with $a = 105$ mm. Each specimen was put into a clamping fixture and then the specimens were loaded, and the load and displacement values were read from the scale of the testing machine and using a digitronic indicator, respectively. The crack initiation was identified visually and when the first non-uniformity in the previously straight crack front was observed, it was believed to be the point of crack initiation.

PELS test

The $\text{PELS}_{\text{I/II}}$ tests were carried out using an Amsler testing machine under displacement control. The crack length of interest was $a = 105$ mm. The critical COD measured from the DCB test[36] is about 15 mm (if $a = 105$ mm). Six steel rollers were used including the following diameters: $d_0 = 6$, 7, 8, 10, 12, and 13 mm. It was assumed that the CODs (δ_{DCB}) were identical to these values. The specimen arms transmitted a relatively high pressure to the steel roller; therefore, the position of the rollers was always stable and no slip along the x axis was observed during the measurements. Similar to the ELS tests, we applied four coupons at each steel roller. The load–deflection data was measured by using the scale of the testing machine and a digitronic indicator. In each case, the critical load at crack initiation was determined.

Results and discussion

It will be shown subsequently that the stiffness, the compliance, and the mode-II ERR of the $\text{PELS}_{\text{I/II}}$ specimen are identical to those of the ELS specimen.

Load and displacement

Figure 6(a) shows a recorded load–displacement curve for the $\text{PELS}_{\text{I/II}}$ specimen in the case of $d_0 = 10.0$ mm. The response follows essentially a linear relation. The $\text{PELS}_{\text{I/II}}$ test was performed according to the following procedures. The onset of crack advance was identified by visual observations. In each case, four specimens were tested, and one of them was used to investigate the crack front. The other three specimens were loaded continuously and the crack initiation was observed *in situ*. Thus, the former specimen was loaded subsequently, at some points where the initiation was expected the specimen was relieved, and removed from the rig, and the crack front was photographed. When the first non-uniformity was observed, this point was denoted as the point of fracture initiation. The results of this process are demonstrated in Figure 6(b) for the $\text{PELS}_{\text{I/II}}$, when the diameter of the prestressing roller was $d_0 = 10.0$ mm.

Table 4 shows that the slopes of the load–displacement traces of the ELS ($d_0 = 0$) and $\text{PELS}_{\text{I/II}}$ specimens are eventually the same. Consequently, the prestressed state does not influence the stiffness of the system noticeably, and the compliance of the $\text{PELS}_{\text{I/II}}$ can be assumed to be equal to that of the ELS system. The maximum difference is 8.6% between the measured and calculated slopes. On the other hand, the results in Table 5 confirm that the effect of friction between the steel roller and the specimen arms on the load–displacement response of the system is insignificant.

Data reduction

Two reduction techniques (IBT and direct beam theory (DBT)) were applied to reduce the experimental data. In a relevant work[25] for the mixed-mode I/II version of the PENF specimen, four reduction schemes were utilized: IBT, simple beam theory, DBT,[37] and the compliance calibration (CC). For mode-I and mode-II specimens, the CC is thought to be the most accurate one; however, its application requires much experimental work. That is why the IBT is the optimal solution in unidirectional composites.

Improved beam theory. *Double-cantilever beam*: In Equation (6), P_{DCB} should be replaced with P_{I}

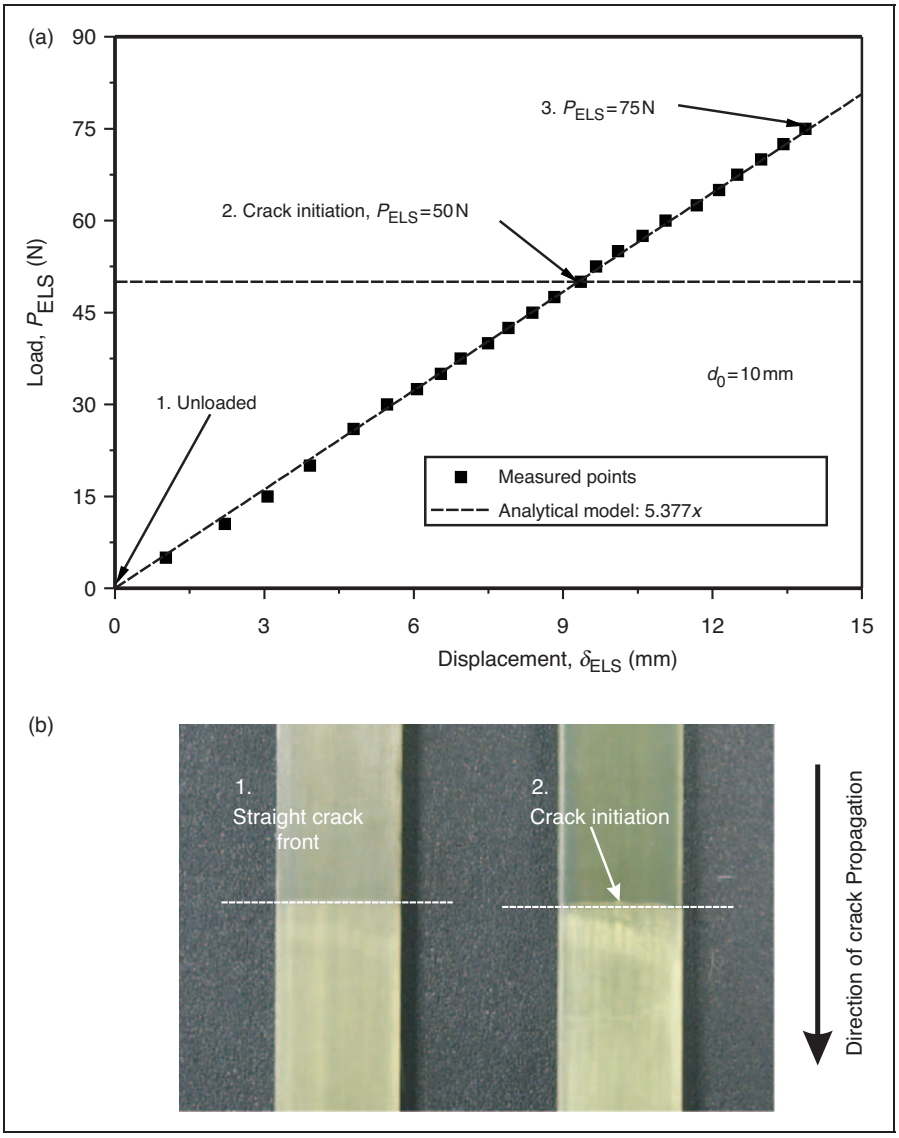

Figure 6. Load–displacement curve of the $PSCB_{I/III}$ system if $d_0 = 10$ mm (a). The identification of crack initiation during the fracture process (b).

(the load value at crack initiation in the DCB specimen) in order to obtain the improved analytical expression for the ERR of the DCB specimen ($G_{IC} = 412\,J/m^2$ from IBT[36]).

ELS specimen: Replacing P_{ELS} with P_{II} in Equation (11) gives the improved solution for the ELS coupon, where P_{II} is the critical load value at crack onset. The IBT resulted in $G_{IIC} = 707 \pm 33\,J/m^2$.

PELS specimen: The improved analytical solutions are given by Equations (9) and (11) for the $PELS_{I/II}$ system.

Direct beam theory. *Double-cantilever beam*: For the DCB specimen, we replace the result of DBT with the one by IBT ($G_{IC} = 412\,J/m^2$).

ELS specimen: In accordance with DBT, it is possible to obtain the following scheme for the ELS specimen:[37]

$$G_{DBT} = \frac{9P_{II}\delta_{ELS}a^2}{2b(3a^3 + L^3)}. \quad (13)$$

where P_{II} and δ_{ELS} are the experimentally measured load and displacement values at the point of crack initiation in the ELS specimen.

PELS specimen: We obtain the DBT scheme for G_{II}, the $PELS_{I/II}$ system if we replace P_{II} with P_{ELS} in Equation (13) (G_I is calculated by IBT). A significant advantage of the DBT is that there is no need to determine the elastic properties of the material.

Table 4. The changes in the slope of the load–displacement curves of the $PELS_{I/II}$ specimen with the roller diameter

d_0 (mm)	0	6	7	8	10	12	13
Load–displacement curve slope-1 (N/mm)	5.5	5.4	5.6	5.5	5.2	5.3	5.7
Difference compared to 5.377 N/mm[a]	1.6	0.6	3.6	1.6	−3.6	−1.9	5.2
Load–displacement curve slope-2 (N/mm)	5.0	5.1	5.4	5.7	5.4	5.5	5.8
Difference compared to 5.377 N/mm[a]	−7.7	−5.5	0.5	5.3	1.1	2.2	8.6

[a]Result of the analytical model.

Table 5. Critical ERRs in the $PELS_{I/II}$ specimen calculated by DBT

	d_0 (mm)	0 (ELS)	6	7	8	10	12	13	~15 (DCB)
	G_I/G_{II}	0.00	0.10	0.21	0.37	0.91	3.17	6.91	∞
		–	±0.01	±0.02	±0.03	±0.16	±0.93	±0.86	–
DBT	G_I (J/m^2)	0.0	51	70	92	143	206	242	412 (IBT)
	G_{II} (J/m^2)	735	490	334	251	157	65	35	0.0
		±52	±36	±28	±23	±24	±19	±4	–
	G_T	735	541	404	342	300	271	277	412 (IBT)

Critical ERRs

The critical mode-I, mode-II, and the mixed-mode I/II ERRs at crack initiation and the mode mix calculated by the IBT are given in Table 3. The geometries tested had properties of $a = 105$ mm, $2h = 6.2$ mm, and $L = 150$ mm, and at each value of the diameter of the prestressing roller (d_0) four coupons were used. Table 5 presents the results obtained by the DBT scheme. In fact, the scatter of the mode-I ERR component is zero; this is because the mode-I ERR is provided by the preload of the specimen. Otherwise, the mode-I components were substituted by the results of the IBT scheme. Comparing Tables 3 and 5, it is elaborated that the difference between the G_{II} values – as well as the mode ratio – by DBT and IBT decreases with the roller diameter (which is eventually equal to the COD). Furthermore, the DBT method gives G_I and G_{II} values which are closer to the maximum values calculated by the FE model. The mode ratio is predicted by both methods in an equally accurate manner.

It is important to recommend a data reduction technique for the $PELS_{I/II}$ system. The reliability and simplicity of the IBT has already been highlighted by other authors.[37,38] On the other hand, the application of the FEM as a data reduction method requires large computational time. Although the DBT method agrees quite well with the VCCT method, at the midpoint of the crack front the IBT seems to be more conservative method in each mode ratio. At this stage, the optimal solution is the application of IBT for the evaluation of both the mode-I and mode-II ERRs; however, the theoretically possible errors should be considered (section 2 and Table 3).

Fracture envelopes

In order to construct a fracture envelope in the G_I–G_{II} plane, we apply two criteria. In accordance with the traditional power criterion, the following relation may be established between the mode-I and mode-II ERRs:[39, 40]

$$\left(\frac{G_I}{G_{IC}}\right)^{p_1} + \left(\frac{G_{II}}{G_{IIC}}\right)^{p_2} = 1. \quad (14)$$

Williams' criterion[39] recommends the following expression for the establishing relation between the mode-I and mode-II ERRs:

$$\left(\frac{G_I}{G_{IC}} - 1\right)\left(\frac{G_{II}}{G_{IIC}} - 1\right) - I_i\left(\frac{G_I}{G_{IC}}\right)\left(\frac{G_{II}}{G_{IIC}}\right) = 0, \quad (15)$$

where I_i is the interaction parameter between the mode-I and mode-II ERRs. If $I_i = 0$, then there is no interaction. Also, if $I_i = 1$, then Equation (15) states a simple addition. In Equations (14) and (15), G_{IC} is the critical ERR under pure mode-I (calculated from the data of the DCB specimen) and G_{IIC} is the mode-II critical ERR (calculated from the data of the ELS specimen). The results of the $PELS_{I/II}$ test listed in Table 3 (IBT) were used to provide six additional points in the G_I–G_{II} plane. The power parameters (p_1, p_2) in Equation (14) and the interaction parameter (I_i) in Equation (15) were determined by a curve-fit technique by applying the OriginPro 7.0 code.

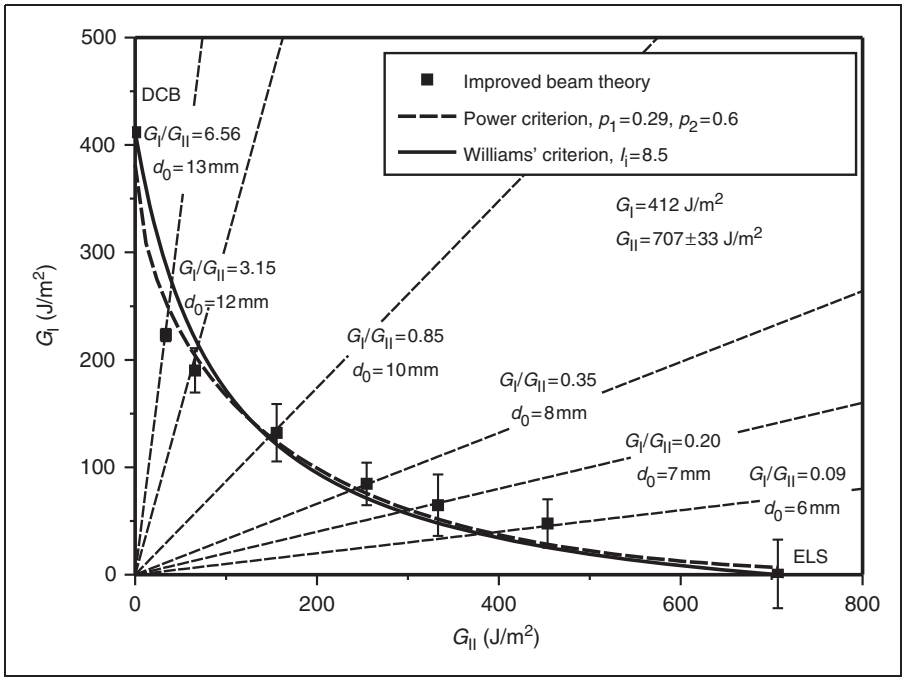

Figure 7. Interlaminar fracture envelope in the G_I–G_{II} plane for E-glass–polyester composite material calculated by the IBT method.

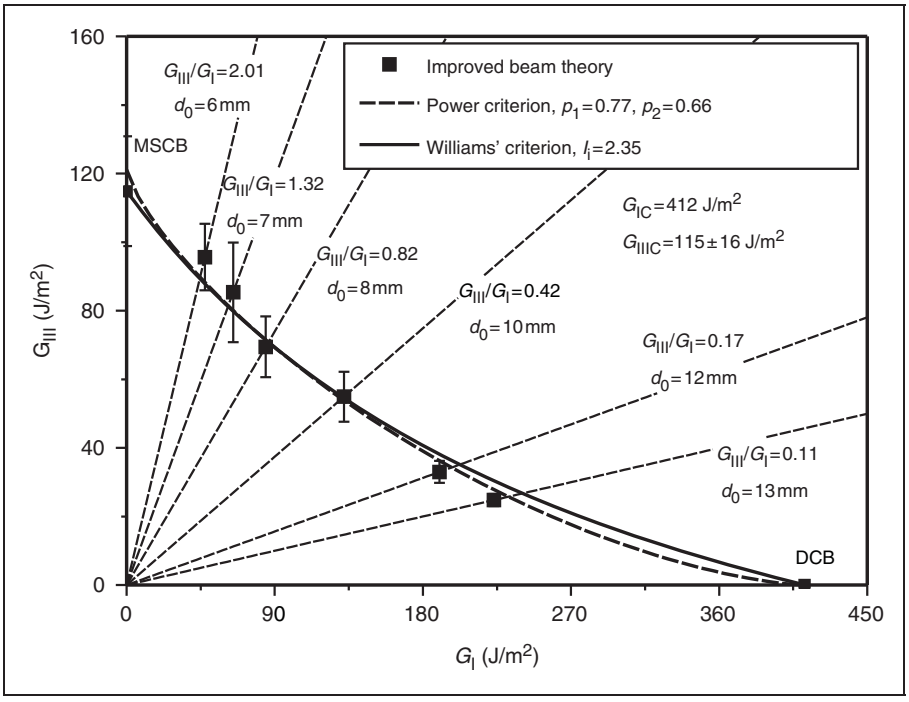

Figure 8. Interlaminar fracture envelope in the G_I–G_{III} plane for E-glass–polyester composite material calculated by the IBT method.

The fracture envelope calculated by the IBT method is displayed in Figure 7. The main conclusion is that there is some interaction between the mode-I and mode-II ERRs. The scatter is also in reasonable ranges. Overall, the difference between the power and Williams' criteria is negligible; both describe the same failure locus.

In a recent work, the fracture envelopes in the G_I–G_{III} plane were constructed by the mixed-mode I/III pre-stressed split-cantilever beam $(PSCB)_{I/III}$ specimen for

the same E-glass–polyester material.[27] A similar experimental study resulted in a convex envelope in the G_I–G_{III} plane as it is shown in Figure 8. Based on the comparison between Figures 7 and 8 we may conclude that the material proves similar behavior in the G_I–G_{II}, and the G_I–G_{III} plane, since interaction takes place in both cases.

Conclusions

In this study, the mixed-mode I/II version of the PELS specimen was developed for interlaminar fracture testing of laminated transparent composite materials. Apart from the ELS and the traditional DCB tests, the $PELS_{I/II}$ specimen was used to obtain the mixed-mode I/II ERR at crack propagation onset including six different mode ratios. To perform the experiments, unidirectional E-glass–polyester specimens were manufactured. An improved beam model was recommended for the evaluation of both the mode-I and mode-II ERRs.

A FE analysis was performed and it was shown that the mode ratio changes along the specimen width and it is not possible to eliminate this variation. The beam theory expressions give approximately the widthwise average value of the ERRs and mode ratio compared to the FE results. In this respect, some assumptions were made considering the data reduction, namely the widthwise average values were believed to give acceptable and realistic results. To assess the possible errors committed through these assumptions, a FE analysis was performed using the VCCT. The crack initiation was expected at the point where the maximum of the total ERR was calculated and the values of G_{II} and G_I/G_{II} were compared to the widthwise average values. The possible errors were estimated to be at most 11.9% in G_{II} and 15.6% in G_I/G_{II}; however, these differences are the results of the rounding.

Based on the performed experimental study, the fracture envelope of the present material was determined indicating a significant interaction between G_I and G_{II}.

The $PELS_{I/II}$ specimen offers several advantages. First, it incorporates the traditional beam-like specimen geometry. Second, it was shown that the $PSCB_{I/II}$ specimen is able to produce any mode ratio at crack propagation onset. The drawbacks of the $PELS_{I/II}$ specimen are that the mode ratio changes with the crack length and the applied load; so the method is recommended mainly for the testing of transparent composite materials. Moreover, the mode ratio changes even along the crack front. Finally, the mode ratio cannot be calculated without performing experiments (i.e., it cannot be designated before the test), involving the fact that the mode ratio will depend on the definition of the crack initiation and the accuracy of the measurement of the load and crack length.

Acknowledgments

The author is grateful to his father (András L. Szekrényes) for the construction of the experimental equipments.

Funding

This work was supported by the János Bolyai Research Scholarship of the Hungarian Academy of Sciences and the National Science and Research Fund (OTKA) [grant number T34040].

References

1. Anderson TL. *Fracture mechanics – fundamentals and applications*, 3rd ed. Boca Raton, London, New York, Singapore: CRC Press, Taylor & Francis Group, 2005.
2. Brunner AJ and Flüeler P. Prospects in fracture mechanics of ''engineering'' laminates. *Eng Fract Mech* 2005; 72: 899–908.
3. Brunner AJ, Blackman BRK and Davies P. A status report on delamination resistance testing of polymer–matrix composites. *Eng Fract Mech* 2008; 75: 2779–2794.
4. Adams DF, Carlsson LA and Pipes RB. *Experimental characterization of advanced composite materials*, 3rd ed. Boca Raton, London, New York, Washington: CRC Press, 2003.
5. Ratcliffe JG. Characterization of the edge crack torsion (ECT) test for mode III fracture toughness measurement of laminated composites. NASA/Technical Memorandum-2004-213269.
6. Rizov V, Shindo Y, Horiguchi K and Narita F. Mode III interlaminar fracture behaviour of glass fiber reinforced polymer woven laminates at 293 to 4 K. *Appl Compos Mater* 2006; 13: 287–304.
7. Yoshihara H. Examination of the 4-ENF test for measuring the mode III R-curve of wood. *Eng Fract Mech* 2006; 73: 42–63.
8. Pennas D, Cantwell WJ and Compston P. The influence of strain rate on the mode III interlaminar fracture of composite materials. *J Compos Mater* 2007; 41: 2595–2614.
9. Morais AB de and Pereira AB. Mixed mode II + III interlaminar fracture of carbon/epoxy laminates. *Compos Sci Technol* 2008; 68: 2022–2027.
10. Morais AB de, Pereira AB, de Moura MFSF and Magalhães AG. Mode III interlaminar fracture of carbon/epoxy laminates using the edge crack torsion (ECT) test. *Compos Sci Technol* 2009; 69: 670–676.
11. Pereira AB and Morais AB de. Mixed mode I + III interlaminar fracture of carbon/epoxy laminates. *Composites Part A* 2009; 40: 518–523.
12. Reeder JR and Crews Jr JH. Mixed-mode bending method for delamination testing. *AIAA J* 1990; 28: 1270–1276.
13. Reeder JR and Crews Jr JH. Nonlinear analysis and redesign of the mixed-mode bending delamination test.

NASA Technical Memorandum 199-1102777, January, pp. 1–49.
14. Tenchev RT and Falzon BG. A correction to the analytical solution of the mixed-mode bending (MMB) problem. *Compos Sci Technol* 2007; 67: 662–668.
15. European Structural Integrity Society (ESIS). Determination of the mixed-mode I/II delamination resistance of unidirectional fibre-reinforced polymer laminates using the asymmetric double cantilever beam specimen (ADCB). Polymers and Composites Task Group, version 00-05-03, 2000.
16. Sundararaman V and Davidson BD. An unsymmetric double cantilever beam test for interfacial fracture toughness determination. *Int J Solids Struct* 1997; 34: 799–817.
17. Sørensen BF, Jørgensen K, Jacobsen TK and Østergaard RC. DCB-specimen loaded with uneven bending moments. *Int J Fract* 2006; 141/1–2: 163–176.
18. Sørensen BF, Jørgensen K, Jacobsen TK and Østergaard RC. A general mixed-mode fracture specimen: The DCB specimen loaded with uneven bending moments. Print. Pitney Bowes Management Services A/S – 2004, Risø-R-1394(EN), pp. 1–35.
19. Chen L, Sankar BV and Ifju PG. Mixed-mode fracture toughness tests for stitched composite laminates. In: *AIAA Paper 2003–1874, Proceedings of the 44th AIAA Structures, Structural Dynamics and Materials Conference*, Norfolk, Virginia, 7–10 April, 2003, p. 10.
20. Arcan M, Hashin Z and Voloshin A. A method to produce plane-stress states with applications to fiber-reinforced materials. *Exp Mech* 1978; 18: 141–146.
21. Choupani N. Experimental and numerical investigation of the mixed-mode delamination in Arcan laminated specimens. *Mater Sci Eng A* 2008; 478: 229–242.
22. Nikbakhta M, Choupani N and Hosseini SR. 2D and 3D interlaminar fracture assessment under mixed-mode loading conditions. *Mater Sci Eng A* 2009; 516: 162–168.
23. Rikards R, Buchholz FG, Wang H, Bledzki AK, Korjakin A and Richard H-A. Investigation of mixed mode I/II interlaminar fracture toughness of laminated composites by using a CTS type specimen. *Eng Fract Mech* 1998; 61: 325–342.
24. Zhang XB, Ma S, Recho N and Li J. Bifurcation and propagation of a mixed-mode crack in a ductile material. *Eng Fract Mech* 2006; 73: 1925–1939.
25. Szekrényes A. Prestressed fracture specimen for delamination testing of composites. *Int J Fract* 2006; 139: 213–237.
26. Szekrényes A. Delamination fracture analysis in the G_{II}–G_{III} plane using prestressed transparent composite beams. *Int J Solids Struct* 2007; 44: 3359–3378.
27. Szekrényes A. Interlaminar fracture analysis in the G_I–G_{III} plane using prestressed composite beams. *Composites Part A* 2009; 40(10): 1621–1631.
28. Ang HE, Torrance JF and Tan CL. Strain energy release rates of interface cracks in orthotropic layered beams. *Int J Fract* 1995; 72(4): 1573–2673.
29. Blanco N, Gamstedt EK, Costa J and Trias D. Analysis of the mixed-mode end load split delamination test. *Compos Struct* 2006; 76: 14–20.
30. Olsson R. A simplified improved beam analysis of the DCB specimen. *Compos Sci Technol* 1992; 43: 329–338.
31. Sorensen L, Botsis J, Gmür T and Cugnoni J. Delamination detection and characterisation of bridging tractions using long FBG optical sensors. *Composites Part A* 2007; 38: 2087–2096.
32. Szekrényes A. Improved analysis of unidirectional composite delamination specimens. *Mech Mater* 2007; 39: 953–974.
33. Rybicki EF and Kanninen MF. A finite element calculation of stress intensity factors by a modified crack closure integral. *Eng Fract Mech* 1977; 9: 931–938.
34. Leski A. Implementation of the virtual crack closure technique in engineering FE calculations. *Finite Elem Anal Des* 2007; 43: 261–268.
35. Krueger R and O'Brien TK. A shell/3D modeling technique for the analysis of delaminated composite laminates. *Composites Part A* 2001; 32: 25–44.
36. Szekrényes A and Uj J. Advanced beam model for fiber-bridging in unidirectional composite double-cantilever beam specimens. *Eng Fract Mech* 2005; 72: 2686–2702.
37. Schön J, Nyman T, Blom A and Ansell H. Numerical and experimental investigation of a composite ENF-specimen. *Eng Fract Mech* 2000; 65: 405–433.
38. Hashemi S, Kinloch J and Williams JG. Mechanics and mechanisms of delamination in a poly(ether sulphone)-fibre composite. *Compos Sci Technol* 1990; 37: 429–462.
39. Hashemi S, Kinloch J and Williams JG. The effects of geometry, rate and temperature on mode I, mode II and mixed-mode I/II interlaminar fracture toughness of carbon-fibre/poly(ether-ether ketone) composites. *J Compos Mater* 1990; 24: 918–956.
40. Reeder JR. An evaluation of mixed-mode delamination failure criteria. NASA Technical Memorandum 1992-104210.